

Utilizing Multi-Temporal Thermal Data To Assess Environmental Land Degradation Impacts: Example From Suez Canal Region, Egypt.

Mohamed Arnous

Suez Canal University Faculty of Science

Basma Mansour (✉ bmhhmg2008@yahoo.com)

Suez Canal University <https://orcid.org/0000-0002-1404-9791>

Research Article

Keywords: Thermal analysis, environmental impacts, waterlogging, salinization, seismic activity, water pollution

Posted Date: January 4th, 2022

DOI: <https://doi.org/10.21203/rs.3.rs-1103079/v1>

License:   This work is licensed under a Creative Commons Attribution 4.0 International License.

[Read Full License](#)

Abstract

Land surface temperature (LST) analysis of Satellite data is critical for studying the impacts of geo-environmental, hydrometeorological, and land degradation. However, challenges arise to resolve the LST and ground field data resulting from the constant development of land use and land cover (LULC). This study aims to monitor, analyze, assess, and map the environmental land degradation impacts utilizing image processing and GIS tools of space-borne thermal data and fieldwork. Two thermal and optical sets of multi-temporal Landsat TM+5 and TIRS+8 satellite data dated 1984 and 2018 were used to test, detect, and map the thermal and LULC change and their land degradation in the Suez Canal region (SCR). The LULC classification was categorized into seven classes: water bodies, urban, agricultural land, barren land, wetland, clay, and salt crust. LULC and LST change detection and mapping results revealed that the impervious surface, industrial area, saline soil, and urban area have high LST, while wetlands, vegetation cover, and water bodies suffered low LST. The spectral, LST profiles and statistical analyses examined the association between LST and LULC deriving factors. The cluster analyses defined the relationship between LST and LC patterns at the LU level, where the fast transformation of LULC had significant changes in LST. According to these analyses and the fieldwork observations, the SCR was divided into six main areas. These areas vary in LST in association with land degradation and hydro-environmental impacts such as rising groundwater levels, salt accumulation, active seismic fault zones, water pollution, and urban and agricultural activities.

Introduction

Globally, environmental land degradation assessment is crucial for the promising economies and societal development as they drive ongoing sustainable development (Arnous et al., 2015; Arnous and Green 2015). Anthropogenic and natural activities are operating not only in the present but also with the past on the surface of the earth as a key driving force of cultural, social, economic development and induce significant environmental changes in the terrestrial ecosystem at various local, regional, and global scales (Xiao et al., 2007; Sun et al., 2012; Zhang et al., 2015; Zhang et al., 2017; Hua and Ping, 2018; Choudhury et al., 2019; Sun et al., 2019). These changes affect the degree of absorption of solar radiation, albedo, surface temperature, evaporation rates, heat transmission to the soil, heat storage, and wind turbulence. Including responsible geo-environmental issues with different contaminants such as water, air pollution, greenhouse gas emissions, and even soil surface temperature (LST) would rise rapidly, which is projected to expose 69% of the world's population by 200 of this vulnerability (Weng et al., 2004, Weng et al., 2006, Mallick et al., 2008; United Nations, 2010; Zhang et al., 2013; Zhang et al., 2016; Pal and Ziaul, 2017; Heinemann et al., 2020). Increasing the demand for the application of modern technology to define, manage, and incorporate environmental and hydro-environmental geospatial data processes is, therefore, important for the overall sustainable development of any country's prerequisites. One of the most important approaches to help decision-makers and environmental planners obtain high accuracy data about environmental land degradation is data analysis of thermal observations. In which the analysis and exploration are attracted approach to detect and assess the land degradation

environmental problems. Also, satellite-based studies will help developers provide recommendations for building design and landscaping major infrastructure projects that are useful in reducing heat accumulation and LULC surface retention. There have been significant developments in the appraisal of land surface environmental circumstances from space-borne satellite data, mostly from thermal infrared remote sensing data. Near-surface temperature and water vapor are of critical significance to investigate of terrestrial hydrology, biospheric processes, and other Earth System Science processes (Prince and Goward 1995; Andersen 1996; Susskind et al. 1997; Dubayah et al. 2000; Arnous and Green 2015; Kalma et al., 2008; Li et al., 2013; Haylemariyam 2018). Remote sensing (RS) and Geographic Information Systems (GIS) technologies have demonstrated their value in mapping patterns in land use/land cover (LULC), geo-environmental effects to track changes in LULC (Hashim et al., 2007; Lilly Rose and Devadas, 2009; Mahmood et al., 2010; Jiang and Tian 2010; Arnous et al., 2011; Tali et al., 2013; Sahana et al., 2016; El-Rayes et al., 2017; Arnous et al., 2017; Igun and Williams 2018; Haylemariyam et al., 2018). RS and GIS integration have been effective in tracking and analyzing LU growth patterns and assessing LU effects on surface temperature. The digital image classification has demonstrated its ability to provide detailed information on the extent, rate, and position of LULC expansion and its related LST rise, especially when coupled with GIS. The alteration of the transition in LC classes on spectral signature and land surface emissivity can be detected by utilizing RS tools. Therefore, the change in LU induced pixels to migrate from cool to hot surface conditions (Jiang and Tian, 2010; Sahana et al., 2016; Haylemariyam et al., 2018). One of the important RS thermal analysis tools in assessing, detecting, and mapping the land–surface physical processes on local and regional scales, particularly in hydrology, meteorology, and the surface energy balance, is remote sensing LST (Czajkowski et al., 2004; Kalma et al., 2008). In modern times, the space-borne data and RS image processing represent a valuable and distinctive tool to acquire the remotely sensed LST over large areas for simple modeling of the dynamic of geo-environmental land degradation impact indicators. Therefore, the multi-temporal RS images can serve as a database for monitoring LULC changes and their dynamics over various time scales in vegetation, water, and urban areas. It also has essential value for using the thermal band to estimate LST (Tali et al., 2013; Igun and Williams 2018; Haylemariyam et al., 2018; Choudhury et al., 2019). Multi-temporal satellite data enables the extraction of LULC and LST information crucial for decision-making on land management, monitoring ecosystems, and sustainable development planning (Coskun et al., 2008; Lilly Rose and Devadas, 2009; Sahana et al., 2016). RS data was useful in the study of the relationships between LULC surface temperature. Currently, the space-borne Thermal Infra-Red (TIR) observations data are an important source to acquire spatially distributed information on the LST, with increasing accessibility and consistency recognitions to the increasing number of launched sensors and developments in processing algorithms (Kuenzer et al., 2013; Li et al., 2013). Therefore, the acquired space-borne thermal observations products have been commonly utilized in the geo-environmental assessment studies such land surface energy budget, water management, drought, urban ecological environment, carbon cycles, land use/ land cover, natural and human disasters that are related to the hydro-environmental and geological events (Cammalleri and Vogt 2015; Haylemariyam 2018; Arnous and Omer 2018). Therefore, LST is significant in relating hydrology and energy balance at the land surface, utilizing its function in evaporation and transpiration processes.

Geo-environmental and sustainable development of the Suez Canal region (SCR), Egypt has been highlighted over the past three decades in the narrow Nile Valley and Delta to relieve the population burden. Therefore, Egypt's government has launched a megaproject called the development project of the century to sustain SCR by turning this investigated area into a major economic zone and prosperous waterfront region to increase the role of the SCR in international trading and develop the Suez Canal Province. In the past decades, many natural and human environmental hazards affected the area under investigation and lead to significant environmental land degradation studied by many researchers such as (Ghodeif et al., 2013, Arnous and Hassan, 2015; Mansour, 2015; Arnous et al., 2015; Geriesh et al., 2015; El-Rayes et al., 2017, Arnous et al., 2017, Geriesh et al., 2019). Therefore, SCR's environmental hazard assessment is important for the environmental analysis and management of this important region to address prevailing environmental hazards, focusing on soil-related issues, climate, tectonic systems, seismicity, flooding, coastal erosion, and soil subsidence and contamination in response to soil degradation. In addition to evaluating the resources and geo-hazard assessment from a geological point of view.

Furthermore, the success of the development plan of an area depends on many factors; the first one is an inventory of rich natural recourses and centers and axes of rapid development, and the second is a reconnaissance of enough reliable environmental data on the natural hazards and the expected hazards produced from the anthropogenic activities. Therefore, applying RS and GIS tools to identify, monitor, evaluate, assess, and map the environmental hazards and LU/LC environmental response change is significant to enhance sustainable development planning within any area worldwide. In the present study, the monitoring and assessing of these environmental land degradation hazards will be accomplished with the utility of RS and GIS tools to define the distribution, nature, magnitude, spatial extent, and temporal activities of land degradation as the source to successful prevention and recovery measures. Several RS and GIS-based analyses of multi-temporal thermal satellite data and the thematic mapping of urban, agricultural activities, groundwater level rising, salt-affected areas, active seismic fault zones, and water pollution hazards have been proposed since the beginning of RS and GIS applied. Hence, the environmental land degradation prints' assessment utilizing image processing and GIS tools of multi-temporal space-borne thermal data and fieldwork verification will be achieved in the present study.

Study Area Characteristics

The study area covers an area of about 10990 km². It is located in the northeastern part of Egypt by geo-coordinates 29° 31'–31° 28' N and 32° 03'–32° 50' E. It is bordered by the Mediterranean Sea to the north and by G. Khashm El-Galala and G. Ataqa to the south. The investigated area is extended for about 25 km to the west and the same distance to the east of the Suez Canal corridor (Fig. 1). The location of the study area lies in the unstable shelf and an active trend. The formations of the unstable shelf are folded and show signs of lateral stress, and its surrounding represent a part of the transitional zone between the Gulf of Suez taphro-geosyncline and the unstable shelf of the northern part of Egypt. (Said, 1962; Smith, 1984; Aboulela, 1994; Badawy, 1996; Hagag, 2016). It is characterized by extensive water

surfaces mainly the Gulf of Suez rift, Bitter Lakes, Lake El Timsah, and Lake Manzala as tectonic depressions responsible for most of the World's Lakes (Holmes, 1965). SCR is covered by sedimentary rocks that belong to the Cretaceous, Middle, Eocene, Late Eocene, Oligocene, Early Miocene, Middle Miocene, Late Miocene, and Pleistocene ages. It is characterized mainly by geomorphological features such as highly topographic mountains, slopes, lowlands, lakes, waterlogged areas, marshes and sabkhas, drainage, sand dunes, wadi depression features. Generally, the study area is dominated by low land, sand dunes, and water surfaces.

The mountainous areas are relatively small and extend from the southern part of the study area to G. Shabrawet northwards. It is steep slopes at the north and east that transform into more gentle - slope terrain to the southwest. The terrain is undulated and dissected by the drainage pattern at G. Ataqa (855 m). The northern parts of G. Ataqa are low land with small to moderate hills of different sizes and shapes. The study area's terrain surface is beginning to elevate with G. Geneifa (265 m) and G. Shabrawet (226 m). An arid climate characterizes the SCR climate; hot, dry, and rainless in the summer and mild with some showers in winter. It has mean monthly temperatures range from about 13°C to 29°C in the winter and summer season.

Meanwhile, the average annual rainfall of this region ranges between 0.3 and 0.5 cm. The daily evaporation varies from approximately 1.5 mm to 7.5 mm in December and July, respectively. The evaporation from the surface open water is about 1600 mm/year (Egyptian Meteorological Authority 2006).

Materials And Methods

There are three types of data that were used to achieve the main aim of the current study such as RS data (Landsat satellite images), geo-referenced (geological, geomorphological maps), and tabular data (field and laboratory measurements). To assess the LULC changes, environmental land degradation and estimate the effects of these changes on LST, the digital image processing methods were used to enhance multi-temporal Landsat series (Thematic mapper (TM), Operational Land Imager (OLI) and Thermal Infrared Sensor (TIRS)) and other RS data to produce various LST thematic maps (Fig. 2). RS methods include selecting optimal bands of thermal spectrum emission compared to other spectral wavelengths to identify the best results for monitoring and assessing wasteland areas and the environmental impact hazard indicators.

The present study's available multi-temporal data is represented by three full scenes of each TM+4 and OLI+8 and TIRS +8 images, scene numbers (Path/Row = 175-38, 175-39 and 174-40), dated 1984 and 2018 respectively (Fig. 3a & 3b). The thermal infrared bands of these data (TM data the wavelength used for LST are band 6, while TIRS +8 of bands 10 and 11) show the infrared radiant's quantity emitted from dissimilar land surfaces. The image was enhanced by utilizing ENVI, ERDAS Imagine, and ArcGIS software. The atmospheric correction was done to reduce the noise effect using the FLAASH module. The multi-temporal RS data was radiometrically and geometrically corrected (UTM zone 36 North projection)

to precise the uneven sensor reaction over the image; and correct the satellite's geometric distortion data (Arnous and Green 2015; Arnous 2016). Furthermore, the thermal and spectral response patterns using multi-temporal and multi-spectral measurements of various terrain features are necessary to collect preliminary information on LULC and the environmental impact degradation, such as waterlogging, salt-affected soils, water pollution, tectonic activity, water content, etc. Image enhancement, including contrast stretching, best band combination, and principal component analysis, were used to produce high spectral resolution images required to detect and monitor land degradation environmental impact hazards from 1984 to 2018 (Fig. 2).

Moreover, the multi-temporal RS data is used for image classification as a method for LU/LC classification by using ENVI and ArcGIS software. In the present study, a supervised image classification of the parametric rule depends on the pixel with maximum likelihood classification has been applied due to the capability to assume the statistics for each class in each band is normally distributed that in turn calculates the probability that a given pixel belongs to a specific class. All pixels are classified only when a probability threshold is selected. Every pixel with the highest probability will be assigned to the class (Pal and Ziaul, 2017; Hua and Ping, 2018). Moreover, the pixel derived from the multi-temporal classified satellite images is utilized to compare similar sites during the field observation and field measurements. Accuracy assessment to the supervised multi-temporal satellite data was carried out, where the accuracy assessment results will provide the users an overall accuracy of the classified map and each class within it. The change detection techniques are used to carry out a qualitative and quantitative evaluation for the multi-temporal thermal and LULC classified images. In the present study, the post-classified comparison technique is applied for two different classified images within timespan of 34 using cross-tabulation. The overall LULC changes are calculated to show the rate of changes for each LULC class and its environmental impacts.

Estimation and construction of the multi-temporal LST maps

The band pixel has a digital number (DN) value in raw RS data connected to a raw measure the sensor acquires. Therefore, the DN has to be converted into physical quantities, radiance, and brightness temperature to obtain quantitative information from raw satellite data.

Correcting the previously calibrated images by atmospheric effects is essential because the atmosphere effect can cause significant distortions in the radiometric signal. Hence the methods used to measure, extract, and map LST from RS satellite data's thermal bands were followed by detecting the geospatial relationships between SCR changes LULC and LST. The following measures were applied to detect the final LST map such as measurement of the Normalized Difference Vegetation Index (NDVI), the conversion of TIRS band data to TOA spectral radiance, and the measurement of atmospheric brightness. Besides, measure LST and determine the area for various ranges of temperatures. Convert LST data from kelvin to centigrade size, finally.

Calculation steps are as follows according to (Xiaolu Zhou and Yi-Chen Wang 2010; Anandababu et. al 2018):

(1) Top of Atmosphere (TOA) Radiance: Using the radiance rescaling factor, Thermal Infra-Red DN can be transformed into TOA spectral radiance as:

For Landsat+5 (TM) data:

$$L\lambda = ((LMAX\lambda - LMIN\lambda) / (QCALMAX - QCALMIN)) * (QCAL - QCALMIN) + LMIN\lambda \quad (1)$$

Where:

$L\lambda$ = Spectral Radiance at the sensor's aperture in watts/ ($m^2 * ster * \mu m$)

$LMIN\lambda$ = the spectral radiance that is scaled to QCALMIN in watts/ ($m^2 * ster * \mu m$)

$LMAX\lambda$ = the spectral radiance that is scaled to QCALMAX in watts/ ($m^2 * ster * \mu m$)

QCALMIN= the minimum quantized calibrated pixel value (corresponding to $LMIN\lambda$) in DN

QCALMAX= the maximum quantized calibrated pixel value (corresponding to $LMAX\lambda$) in DN

For Landsat+8 (OLI/TIRS) data:

$$L\lambda = ML * Qcal + AL \quad (2)$$

Where: $L\lambda$ = TOA spectral radiance (Watts/ ($m^2 * sr * \mu m$)), ML = Radiance multiplicative Band (No.), AL = Radiance Add Band (No.) and Qcal = Quantized and calibrated standard product pixel values (DN).

(2) Top of Atmosphere (TOA) Brightness Temperature: Spectral radiance data can be transformed to top of atmosphere brightness temperature using the thermal constant Values in Meta data file.

$$BT = K2 / \ln (k1 / L\lambda + 1) - 272.15 \quad (3)$$

Where: BT = Top of atmosphere brightness temperature ($^{\circ}C$), $L\lambda$ = TOA spectral radiance (Watts/ ($m^2 * sr * \mu m$)), K1 = K1 Constant Band (No.) and K2 = K2 Constant Band (No.)

(3) Normalized Differential Vegetation Index (NDVI): The NDVI is a standardized vegetation index that estimated using Near Infra-red and Red bands.

$$NDVI = (NIR - RED) / (NIR + RED) \quad (4)$$

Where: RED= DN values from the RED band NIR= DN values from Near-Infrared band

(4) Land Surface Emissivity (LSE): LSE is the average emissivity of an element of the surface of the Earth calculated from NDVI values.

$$PV = [(NDVI - NDVI \min) / (NDVI \max + NDVI \min)] ^2 \quad (5)$$

Where: PV = Proportion of Vegetation, NDVI = DN values from NDVI Image, NDVI min = Minimum DN values from NDVI Image, NDVI max = Maximum DN values from NDVI Image, $E = 0.004 * PV + 0.986$
Where: E = Land Surface Emissivity and PV = Proportion of vegetation

(5) Land Surface Temperature (LST): The LST is the radiative temperature that calculated utilizing Top of atmosphere brightness temperature, Wavelength of emitted radiance, Land Surface Emissivity.

$$LST = (BT / 1) + W * (BT / 14380) * \ln(E) \quad (6)$$

Where: BT = Top of atmosphere brightness temperature (°C), W = Wavelength of emitted radiance and E = Land Surface Emissivity.

(6) Convert of LST data to centigrade scale: It will obtain by using this equation

$OC = T - 273.15$ where T=at satellite temperature computed from equation 3 for both Landsat+5 TM and Landsat +8 OLI/TIRS sensors.

Cluster analysis

The cluster analysis classification technique is generally placing objects into homogeneous groups to reveal the relation between groups. This technique is designed to select subsets of mutual elements from the matrix of many such elements (Variables or classes). Furthermore, it considers a similarity matrix developed from the new data matrix and defines pair by pair the inter-correlation of variables (R-mode) or cases (Q-mode) in a two-dimensional hierarchical diagram called the dendrograms Harbuaugh and Marreium, (1968). The Euclidean distance provides a reliable measure of the actual similarities between samples or classes. After comparing the LST images and the LULC classification images and determining the temperature ranges of each LULC class (Fig. 2), the change behavior and relationship between the LULC classes in a time span of 34 years can be clearly understood based on land surface temperature changes using the cluster analyses. The cluster analysis done in the present work is based on the Ward method, where the distance metric is Euclidean distance and depends on the maximum, minimum and mean values of temperatures in each given LULC class.

Across the SCR area, four profiles have been made to represent the variations of LST and LULC reflectance between all major classes within 34 years. Moreover, according to the type of hydro-environmental impact and land degradation, the SCR was divided into six hot spots, later on, showing the change in the extent and spatial distribution within the time span of 34 years of the satellite data due to the natural and/or human activities, particularly agricultural, industrial, and urban activities. Field measurements also included water level and salinity surveys for 5 points east of Bitter lakes to confirm the results deduced from LULC and LST changes by comparing them with previous literature (Geriesh 2003). Both electric sounder and EC meter were used to make water level and salinity surveys, respectively.

Results And Discussion

Operational and sustainable human activities management progressively need advanced techniques to obtain numerous and up-to-date information on the pattern, state, characteristics, and development of an urban environment. Today, the satellite observations data is considered an effective data source for environmental analysis that is essentially well-matched to offer information on LULC characteristics and their environmental impact changes over time at various spatial and temporal scales. Therefore, there have been significant advances in estimating land surface environmental conditions from satellite observations, mainly from thermal infrared remote sensing data. Near-surface temperature and water vapor are of critical importance to investigate and assess the geo-environmental impact hazards. With the development and innovations in earth observation data, technologies, and theories in the broader field of earth observation, and environmental remote sensing has quickly increased popularity among a wide variety of communities from several aspects as LU/LC mapping, LST analysis, impermeable surface area estimation and geo-environmental safety assessment, which will be illustrated in the following sections:

LULC types and areal change analysis

The LULC classification has been carried out for the multi-temporal Landsat satellite data for the last four decades in the current work. The LULC classification has been categorized into seven classes viz. water bodies (waterlogged, lakes, sea, fish farm, and canal), urban (Residential, industrial, and commercial zones), agriculture (high and low density) land, bare (Sand dunes, sand sheet, and mountainously areas) wetland, clay, and salt crust (Fig. 4a&b). The accuracy assessment for the LULC classified maps was analyzed. The accuracy assessment results will give the users an overall accuracy of the map and an accuracy for each class in the obtained classified map. Therefore, the pixels derived from the images were used to compare similar sites in this field.

Furthermore, validate the classified maps the random points for TM 1984 and OLI 2018 have been collected from Google Earth images. The overall accuracy percentage for classified images were for the TM 1984 is 91.7, and for OLI 2018 is 90.10. The results' reliability was derived with the help of the Kappa coefficient, and the values of the Kappa coefficient are 0.92 and 90 for the TM 1984 and OLI 2018. The pattern and spatial distribution of LULC changes were shown by preparing the multi-temporal LULC maps. The areal distribution of LULC changes was shown in Table (1).

Table 1
The results of change detection of land-use/landcover between 1984 and 2018.

Class	Surface area in 1984 (km ²)	Surface area in 2018 (km ²)	Difference (km ²)	Average yearly rate of change (km ² /year)
Wetlands	275.44	26.86	-248.58	-7.31
Urban areas	26.21	151.1	+124.89	+3.67
Clay	204.04	199.34	-4.7	-0.138
Water bodies	2009.24	1935.67	-73.57	-3.06
Salt crust	567.75	278.26	-289.49	-8.51
Vegetation	306.67	1215.36	+908.69	+26.72
Baren areas	6,530.87	6,113.63	-417.24	-12.27

There is a significant increase in the urban area, including settlement and industrial, from 26.21 km² to 151.10 km². Also, there was a significant increase in vegetation, including dense and scattered vegetation, from 306.67 km² to 1215.36 km².

While the salt crust decreased from 567.75 km² to 278.26 km². Along with LULC changes, the rate of change has been calculated for a time span of 34 years to depict which LU types are converting very rapidly to other LU types (Table 1). The obtained results indicated that the majority of the barren land area was converted into agriculture and urban with an average rate of change +26.72 and +3.67 km²/year, respectively. Simultaneously, the same situation happens to the clay and salt crust areas, which reduced from 204.04 to 199.34 km² and 567.75 to 278.26 km² respectively, to transform into fish farms and vegetation land with an average rate of change -0.138 and -8.51 km²/year, respectively. Nevertheless, the wetland area was detected to have changed drastically for a time span of 34 years, whereas the area declined from 275.44 km² to 26.86 km² with a rate of change -7.31 km². The water bodies decreased in area from 1984 to 2018 as -73.57 and the change rate -3.06 km²/year due to the shrinkage of Al- Manzala and Al- Malha lakes (Fig. 4a & 4b). Overall, the SCR's sustainable development is founded to have occurred and continuously lead to some environmental issues. The main issue causing uncontrolled rapid urbanization and land reclamation was the demand for LU for human activities such as residential, industrial, commercial, other concrete buildings, and agricultural activities. Therefore, most of these LULC developments lead indirectly to environmental and land degradation hazards such as increased salinization processes, pollution of water, soil, and waterlogging (Fig. 5).

Moreover, according to the change detection calculations of the obtained LULC maps of SCR, we observed that the study area had changed drastically for the last four decades whereas 50% of SCR is increased and 50% of SCR is decreased (Table 1). These SCR land surface changes are subjected to the human and natural activities for sustainable developments and their environmental land degradation processes.

Multi-temporal thematic thermal maps and their distribution

In the present study, LST was derived from multi-temporal Landsat satellite data (TM 1984 and OLI/TIRS 2018). The thermal band of TM+5 and TIRS+8 was used to map the SCR region's thermal distribution anomalies. The LST was estimated using the conversion of radiance to AT satellite brightness temperature and spectral emissivity. Figure (6a) shows the calculated LST of the SCR region. Table (2) shows that the maximum temperature of TM 1984 recorded was 59.8°C and a minimum temperature value of 5°C.

On the other hand, on OLI/TIRS 2018 (Fig. 6b), the highest temperature value recorded was 57.38°C and the lowest temperature was 13°C OLI/TIRS 2018. Therefore, the average LST of the area for thermal multi-temporal data within a time span of 34 years has increased from 31.97°C to 43.92°C with an LST change of 0.352°C per year, which reveals that the SCR is facing many environmental changes according to LULC changes. Table (2) shows the estimated values of seven major LULC classes; It reveals that the clay, wetland, urban, and salt crust areas in 1984 exhibited the highest LST having a mean value of 45.7°C, 41.43°C, 35.46°C, and 33.46°C, respectively. However, barren land, water bodies, and vegetation have lower LST, with a mean value of 21.5°C, 22°C, 24.27°C, respectively. Moreover, the statistical estimated LST values in 2018 show that the LST values of clay, salt crust, wetlands, and urban areas exceed other LULC classes with a mean value of 51.69°C, 47.29°C, 45.20°C, and 44.90°C, respectively.

On the other hand, water bodies show the lowest LST values having a mean of 35.37°C. Other scholar has also witnessed that the highest values of LST are in the urban area and other impervious surface, while the lower LST values are found around vegetated and barren, lands areas. Within the time span of 34 years, the agricultural and reclaimed land activities in SCR have been increased. Therefore, the vegetative covers absorb heat during the daytime and release it at night; thus, LST's low values is commonly recorded in such LULC class. The temperature value around dry saline soil, residential, industrial, roads, and concrete pavements become considerably higher than bare land. However, waterlogged, surface water, and wetland show relatively low LST value in the study area. Results of LST change detection between 1984 and 2018 (Fig. 6c) showed that the whole area has increased in temperatures (red color) except for the southern part of El-Manzala lake and Sahl El-Tina plain (blue color) in the west and east of the Suez Canal, respectively as a direct impact of El-Salam Canal construction in 2003. El-Salam Canal gets its water from the Nile and passes under the Suez Canal through a siphon to deliver fresh water to Sinai. This canal intercepted the groundwater flow to the northern area of El-Manzala lake and the sea, increasing the water levels in the southern area (Mansour 2015), consequently lowering its LST. On the other hand, the availability of water in Sahl El-Tina plain

after 2003 has led to major humanmade activities (agriculture and fish farming) on this plain's clay soil nature. The faulty agriculture water drainage has led to the rising of the waterlogging problem in this area. Consequently, the land-use changes in the Sahl El-Tina plain have lowered the LST of this area. Also, the construction of the second Suez Canal branch in 2014 has lowered the LST in this area, confirming the power of land-use changes over LST.

Finally, the agriculture expansion on El-Salheya plain of relatively higher land elevation from its surroundings has led to the infiltration and flow of irrigation water to the lowlands of the El-Ballah area, which acts as a discharge zone for the whole Ismailia governorate in the west of the Suez Canal (Mansour 2015), thus, Lowering the LST in this area (Fig. 6c).

Table 2

The results of land surface temperature changes in land-use/landcover classes between 1984 and 2018.

Class	Temperature ranges in 1984 (°C)	Temperature ranges in 2018 (°C)	Mean Temperature in 1984	Mean Temperature in 2018
Wetlands	12.48 - 57.88	31.26 -56.05	41.43	45.2
Urban areas	8.6 - 53	31.24 -56.51	35.46	44.9
Clay	18.59 -59.8	34.52 -56.88	45.7	51.69
Water bodies	5 - 48.73	13 - 57.38	22	35.37
Salt crust	7.5 - 55.9	31.38 -56.76	33.46	47.29
Vegetation	9.75 - 42.89	13 - 57	24.27	42
Baren areas	5 - 48	33 - 49	21.5	41

Relation between LST, LULC classes and change detection of the land degradation hazards

Comparing the LST images and the LULC classification images, the relationship between the LULC classification and the LST can be clearly understood. The terrestrial change of LST has changed over with speedy LULC changes within 34 years timespan. Across the SCR area, Cluster analysis between 1984 and 2018 LST ranges for LULC classes and four cross-sections have been made to represent the variations of LST between all major classes (Figs. 7 and 8, respectively). Cluster analysis was successfully used to classify LULC and determine the LST groups of distinct populations that may be significant in the land degradation for the obtained results of enhanced satellite data of 1984 and 2018. The R-mode dendrogram of the LST variables of the LULC in SCR was construed and displayed in two main clusters (Fig. 7).

In 1984 (Fig. 7a), the first cluster group was clay with the salt crust, and urban may point to high LST values. The second cluster has vegetation with bare land, water bodies, and wetlands pointing to lower LST values. Figure (7a) shows the natural response of different classes to LST values, as the salt crust and urban areas usually have the same spectral signatures and LST, hence clustered in the same group with high LST of the clay class. In addition, there is a clear correlation between the other classes showing the effect of shallow groundwater on barren lands and the rest of the classes with lower LST values, thus clustering in the same group.

On the other hand, in 2018 (Fig. 7b), the first cluster group was transformed into vegetation and water bodies, which reveals that the higher vegetation cover helps lower the LST and the increase in the groundwater level. This relationship highlights the increase in agricultural activities as a major source that is a threat to water quality, waterlogging, and salinization. Furthermore, the cluster group found between bare land and clay, salt crust, urban and wetlands may reflect the role of urbanization processes in SCR and increase LST rate, particularly in the impervious surface and saturated saline soils. Hence Figure (7b) reflects the increase of human activities response on the LULC classes' LST. Therefore, four cross-sections have been produced across the SCR area to represent LST variations between all major classes with the LULC transformation as a land surface reflection (Figs. 4 and 8). Generally, the cross profiles reveal an abrupt increase in LST and land surface reflection of the study area. In profile one from E-W, it is demonstrated that the human activities increased based on the LULC changes and due to change of LST values (Fig. 8a and b). It is found that the salt crust, clay, and wetlands on the eastern side of the Suez Canal were transformed into fish farms and agricultural areas. At the same time, on the western side of the Suez Canal, the water body of El-Manzala Lake, bare land, and wetland were transformed into agricultural, industrial, and fish farms. LST also increases and decreases due to the transformation of LULC classes. For example, the salt crust and water bodies recorded maximum LST of 50°C and 20°C in 1984, respectively. These classes were changed in 2018 into fish farms and agricultural areas with recoding LST reaching 55°C and 40°C, respectively. Profile two from NE-SW shows the decline in LST values of salt crust, barren land, waterlogged, and scattered vegetation classes in 1984 (Fig. 8c and d). These classes were transformed in 2018 into dense vegetation, large waterlogged, wetland, and barren land classes. The barren land and salt crust recorded maximum 40°C and 42°C in 1984. These classes were modified in 2018 into agricultural and waterlogged areas with recoding LST as from 48 to 54°C and from 35 to 40°C, respectively.

Moreover, profile no. Three from NW-SE shows the increasing LST values of barren land, particularly mountainous areas, from 1984 to 2018 (Fig. 8e and f). The barren land area recorded maximum 43°C and 46°C in 1984 and 2018, respectively. These changes in LST value may be due to the increase of the seismic activity and sand dune migration that covered the dried natural drainage distributaries in this area. Finally, profile four from N-S indicates the increasing and altering LST values of vast barren land area in 1984 at south bitter lakes (Fig. 8g and h). It was converted in 2018 into dense vegetation, waterlogged, wetland, and urban classes. The barren land area recorded maximum 35°C in 1984. At the same time, its maximum value of the LST barren land was modified and maximum record as 45°C, 32°C, 40°C, and 46°C in 2018 for dense vegetation, waterlogged, wetland, and urban, respectively.

Detecting and monitoring the hydro-environmental impact and land degradation

Visual interpretation of the resulted maps depends on RS image characteristics and prior knowledge of the investigated area. Fieldwork and other ancillary geological and environmental data were carried out to help identify and map environmental land degradation. The multi-temporal optical and thermal satellite data were considered a base map for allocating changed environmental land degradation classes. The multi-temporal hotspots of SCR were mapped using ERDAS Imagine, Envi, and ArcGIS software; six hotspots were chosen to detect and monitor the hydro-environmental impact and land degradation (Fig. 9). The multi-temporal hotspot maps show the change in the extent and spatial distribution within the time span of 34 years of the satellite data due to the natural and/or human activities, particularly agricultural, industrial, and urban activities. Therefore, by comparing the LST images and the LULC classification images, the relationship between the LULC classification and the LST can be clearly understood. The following section will compare different hot spots from the enhanced LST and LULC multi-temporal satellite between 1984 and 2018 to identify the hydro-environmental and land degradation in SCR. These degradations include natural, human activities, water pollution, groundwater level rising, salinity increase, and seismic activity.

At hot spot no. 1, the enhanced multi-temporal LST and LULC images (Figs. 9&10) show that Lake Manzala (LM) and its surrounding area have a significant change in human and natural activities. The water temperature is mostly lower than in other types of LULC. However, the water body proportion, the average size of the water body, isolation, water quality, and water body fragment affect the change in LST values. Hence, the water quality deterioration of LM has changed LST values dramatically. Between 1984 and 2018, LM LST values increased from 5-28°C to 38 - 45°C near the industrial and urban zones. The vast amounts of contaminated wastewater and accumulated bottom sediments near these sites contain heavy metals that could be monitored and detected based on the observation of change in LST values, particularly at the drains. The pattern of surface water temperature changed to circular rims around these areas (Fig. 10). The contaminated water and sediments' heat pockets are indicated by the shades of green and yellow colors in the LST (Fig. 10).

These results agree with Arnous and Hassan (2015); their findings revealed that the water and sediments of LM constitute an ultimate sink for heavy metals in the LM aquatic system. The industrial, agricultural, and domestic wastes, sewage water, and commercial activities; led to a harmful concern for the natural environment of the LM and its surrounding area. Moreover, the southern LM area suffers from an increasing water level due to El-Salam Canal's digging in the last two decades. It prevents the groundwater flow from reaching the northern wetlands as it acts as an artificial barrier (Mansour 2015). This action has led to the transformation of the wetlands to land reclamation, agricultural, urban areas, and fish farms.

At hot spot no. 2 (Figs. 9&11), the LULC of this area at 1984 show that it was mostly covered by clay, salt crust, barren land, and ponds classes, which have LST values ranging from 5 to 64°C. These classes were rapidly reclaimed by several development activities, besides the natural processes and both severely

affected the LU/LC pattern. The transformed LULC classes in 2018 included the saline soils, cultivated lands, salt crusts, waterlogging, barren lands, fish farms, and urban areas (Fig. 11). The main converted classes were saline soils, barren lands, cultivated lands, and fish farms, while salt crusts, waterlogged, and urban areas have small spatial distribution. The detection and the monitoring of the results of environmental impacts and land degradation was based on the change detection of LST values and agree with the results of Arnous et al., 2017; El-Rayes et al., 2017 and Moubarak et al., 2020.

The change of the LST values may be attributed to the dominance of saline soils and barren lands, and to the natural evaporation process acting on the saturated soils, leading to increased soil salinity and increasing LST values from 38-48°C to 47-53°C. Salt crust is mostly located in the middle and the coastal zones under the impact of evaporation of the seawater and waterlogging along the ground surface, associated with LST change values from 33-48°C to 46-50°C.

On the other hand, the agricultural activities and fish farms decrease LST values from 33-48°C to 13-37°C depending on the water's salinity degree. The transformation of agricultural lands may elucidate the significant extent of fish farms after digging Salam Canal. Besides, many waterlogged sites appeared, and the saturated saline soils increased near the cultivated lands and are related to the increasing groundwater level and shallow clay layers. Moreover, the sand dunes class's LST values in 1984 are 33-37°C, which increased after 34 years to 46°C due to migrations of sand dunes covering the vast area of saline soil and clay classes. Also, exposed waterlogged areas have lower LST values ranging from 13 to 32°C less than the sand dunes LST values (46°C). While the area at Malha Lake in 1984 is mostly covered by saline water bodies and saturated soil with LST values 5-32°C, which increased to 46-54°C after being transformed into barren and saline soil after backfilling and draining the primary area of the Malha lake.

At hot spot no. 3, This hot spot is a perfect example to show the effect of shallow water table on surface soil moisture and agricultural activities to detect the depth to water table via retrieval of moisture in the surface soil based on the multi-temporal LST results analyses (Fig. 9&12). it was evident that LULC changes, especially those related to the surface soil moisture, varied extensively in this hot spot, and was confirmed with several studies such as (Mansour 2015; Arnous and Green 2015; Arnous et al., 2015 and Hassan et al., 2019). Therefore, the hydro-environmental information could be acquired or estimated from LST data analyses, such as fluctuation of the water table or water table level rise, which are the primary reason for waterlogging problem occurrence. The least LST values were identified in waterlogged areas 5-24°C in 1984 and 13-32°C in 2018, especially at El-Balah due to change of the source and water quality with the groundwater level rising, increasing the LST of wet saline soil to 29-32°C and LST of the fish farms (13-32°C in 2018). In contrast, the cultivated areas are characterized by low to moderate LST values due to the change in crop type and irrigation systems. The extensive land reclamation and agricultural activities caused the appearance of many hydro-environmental problems such as waterlogging and soil salinization due to irrigation and though rising waterlogged sites by seepage towards low topographic areas. The highest LST values were detected in barren soil (50-57°C in 2018), particularly at El-Salhyia plain due to low vegetation density and well-drained soil. Some sites located at

the eastern side of the new Suez Canal suffered from a change in the LST values from 33-37°C in 1984 to 46-49°C in 2018 due to the increase in evaporation of the heavily moist surface soil. It is worth mentioning that in 1984 there was a large lake east of Suez Canal navigation route with temperature ranges between 21 to 24°C. This lake dried out due to the increase in vegetation crops in this area which is irrigated by mixed fresh and groundwater (pumping from wells dug in the area).

At hot spot no. 4, the LULC and LST multi-temporal maps of this area within the time interval of 34 years shows various consequences, especially in the urban ecosystems east and west of the Suez Canal. LULC classification was acquired to represent unique socio-economic activities based on their environmental land degradation effects and the existing national LULC classification standards. Speedy urbanization driven at or around both Ismailia and New Ismailia Cities by population growth and economic development has severe and extensive modifications to the land surface, causing the replacement of natural surfaces such as vegetation with impervious surface materials such as concrete, asphalt, and buildings. It also transformed the barren land and agricultural area to dry and saturated saline soil and waterlogged areas (Fig. 13). The widespread LULC transformations have created ecological and environmental problems at multiple scales in this hot spot. The LULC of this area in 1984 shows that the urban area of Ismailia City has LST values ranging from 25 to 32°C (Fig. 13). After 34 years, the rapid urbanization such as residential, industrial, parks, and institutional LU and land reclamation to the sustainable development of this hot spot area led to increasing the LST values from 40 to 57°C in 2018. In addition, the barren land (LST values 29-32°C in 1984; 46-57°C in 2018) and agricultural areas (LST values 21-24°C in 1984; 13-35°C in 2018) are transformed into extensive agricultural actions associated with decrease the LST values. These actions lead to some hydro-environmental problems such as increasing the waterlogged areas in the west and east Suez Canal and increasing soil salinization. This agricultural expansion could raise the moisture of the surface soil by irrigation and increase waterlogged areas by seepage towards low laying areas. Therefore, the exposed waterlogged areas have lower LST values ranging from 5 to 14°C in 1984, while LST values in 2018 are increased to 13 – 35°C. It may reveal the increasing water salinity and the widespread of the saturated saline soils associated with groundwater level rising.

Furthermore, the saline areas that transformed into waterlogged in the eolian plain and the windblown deposits, particularly at the southern of Wadi El Tumilat, due to the continuous groundwater level rising. On the other hand, it is a value observing around the new Suez Canal due to the increase in surface soil moisture. These above results agree with many literature reviews such as (Ghodeif et al., 2013; Arnous and El-Rayes 2013; Arnous et al., 2015; Mansour 2015; Arnous and Green 2015; Hassan et al., 2019).

At hot spot no. 5, the LULC of this area at 1984 show that it is mostly covered by urban, barren land, saline soil, and low density of vegetation classes, which have LST values ranging from 5 to 64. These classes are rapidly reclaimed by several development activities, besides the natural processes, severely affected the LU/LC pattern. The transformed LULC classes in 2018 include the saline soils, cultivated lands, salt crusts, waterlogging, barren lands, and extensive urban areas (Fig. 14). The main converted classes were saline soils, barren lands, cultivated lands, and fish farms, while salt crusts, waterlogged,

and urban areas with a small spatial distribution. The change of the LST values may be attributed to the dominance of saline soils and barren lands and to the natural evaporation process acting on the saturated soils, leading to increased soil salinity and is associated with increasing LST values from 21-42°C to 44-53°C within timespan 34 years. Salt crust is mostly located along the coastal zones of the Suez Canal's eastern side, leading to the spreading of the seawater and waterlogging along the ground surface associated with evaporation and impacting the LST change in values from 33-42°C to 46-53°C.

On the other hand, the agricultural activities lead to the decrease in LST values from 33-37°C to 46-49°C depending on the salinity degree of water. The conversion of barren land to agricultural lands and new urban extension, particularly at Suez City, lead to the appearance of numerous waterlogged locations and increasing the saturated saline soils nearest and close to the cultivated lands; may be related to increasing groundwater level and presence of shallow clay layers. The exposed waterlogged sites have lower LST values ranging from 5 to 14°C less than the LST values of the other classes. Moreover, the sand dunes class's LST values in 1984 are 33-37°C, which increased after 34 years to 46°C due to migrations of sand dunes covering the vast area from saline soil and clay classes. While saline water bodies mostly cover the area at the eastern side in 1984, with saturated soil and sand dunes having LST values 21-41°C, which are increased to 44-53°C after being subjected to seismic activities near neotectonics features.

These neotectonics features could be detected and monitored through the analyses of the LST multi-temporal data. The fault plan may offer a perfect avenue to moisture or vegetating growth and may form specific drainage patterns easily detected on the enhanced satellite data. According to the enhanced satellite data results and the epicenters data of this hot spot, there is a sudden change of course of the drainage system with displacement inferring to structural control of the area and the overlay with epicenters around the area. These integrated and overlaid data revealed that the study area was subjected to tectonic activity and active faults based on the detection of some neo-tectonic features and the tracing of some structural tectonic active faults in the SCR area (Fig. 15). Moreover, this area witnesses more urban (settlement and industrial) activities, which increased the LST values from 14-24°C in 1984 to 36 – 40°C in 2018.

At hot spot no. 6, according to the comparison of LST multi-temporal data, there is a high increase in the vegetation cover and land reclamation in most of this hot spot which is intensively cultivated and mostly irrigated. After digging some new canals, there is a decrease in the barren land and the appearance of waterlogged and salinization effecting soils with patchy vegetation. These observed results of the land degradation and hydro-environmental impacts are confirmed with (Arnous 2004 and Arnous et al., 2020). This was associated with changing the LST values from 5-48°C to 13-53°C, related to the major environmental degradation indicator in this arid environment, mainly surface water, waterlogging, and wetlands problems (Fig. 16). Therefore, the enhanced data results reveal a significant decrease and/or increase in the area covered by water bodies. The area of water bodies (LST values 5- 14°C) shows a positive change due to the construction of irrigation canals, drains, and new farms established in recent years resulted from extensive human agricultural activities, mostly related to irrigation. In irrigated areas,

farmers may not control irrigation, which commonly results in excess water being added to the groundwater. Continuous irrigation for further agricultural activities and new land reclamation with excess water induces a rise in the groundwater table especially in areas with shallow clay lenses. The seepage of water creates waterlogging of low-lying areas from irrigated uplands and from the canal system. In addition to transforming the saline saturated soils into dry saline soils, associated climatic change leads to an increase in the LST values of 1984 to 2018 from 33-42°C to 46-53°C.

Table 3
The change in soil water level (perched condition) and salinity between 2003* and 2018.

sample	TDS in 2003 (mg/l)	TDS in 2018 (mg/l)	Water table 2003 (m)	Water table 2018 (m)
1	6300	2400	5.55	3
2	5200	2800	4.7	2
3	3000	5120	3.7	1
4	9800	2260	3.7	1.5
5	12000	3800	6.5	1.5

* Geriesh, 2004

Table (3) and (Fig. 17) sum up the relation between increased agriculture and waterlogging (groundwater rising). Increasing the vegetation cover in the area East of the Bitter Lakes decreased the groundwater levels from the year 2003 to 2018 due to the mixed irrigation between surface (Sinai Canal) and groundwater and over pumping from wells. However, some areas suffered from waterlogging due to the shallow clay layers underneath (return flow) which prevents the vertical percolation of water and increases the surface water salinity due to Evaporation. Deeper groundwater has lower salinity and is less affected by the evaporation process. Where the maximum effective evaporation depth in this area is about 0.6 m below the ground surface (Geriesh 2003).

Conclusion

The present study identifies and assesses a fundamental hypothesis in extensively used geospatial technology to attribute LST anomalies convinced by LULC where the LULC changes are the main driving forces of the environmental land degradation, thus thermal changes deterioration. The current study aims to monitor, analyze, assess, and map the environmental and hydro-environmental land degradation impacts of the SCR employing remote sensing and GIS tools of multi-temporal thermal data and fieldwork. The multi-temporal Landsat TM+5 and TIRS+8 satellite data dated 1984 and 2018, statistical analysis, and fieldwork succeeded in detecting and mapping the multi-temporal LST, LULC change, and their land degradation of SCR. The geospatial distributions of the LST in terms of LULC changes was released based on the multi-temporal thermal data of TM1984 and OLI/TIRS 2018 Landsat data, in

addition to the multi-temporal satellite data has classified into seven major LULC classes as water bodies, urban, agricultural land, barren land, wetland, clay, and salt crust. The results show that, in the last 34 years, the portion of the SCR suffering from a change in land under build-up, vegetation, wetland, salinization, and sand dunes classes. These have shown significant expressions due to human and natural activities. On the other hand, barren land has shown a considerably high conversion rate and decreased territorial extent within this period. LULC and LST change detection and mapping results revealed that the impervious surface, industrial area, saline soil, and urban area have high LST. In contrast, wetlands, vegetation cover, and water bodies have suffered low LST. Therefore, the spectral signature, LST profiles, and the statistical analyses studied the association between LST and LULC deriving factors. In addition to the relationship between LST and LC patterns at the LU level, the fast transformation of LULC had significant changes in LST. The SCR changed areas by the LST are associated with land degradation and hydro-environmental impacts such as groundwater level rising, salt accumulation, active seismic fault zones, water pollution, and urban and agricultural activities. LST, fieldwork, statistical analyses, and their interpretations indicate that the clay class with the salt crust and urbanization shows the highest LST values. Moreover, the vegetation class with bare land, water bodies, and wetlands pointing to lower LST values. The salt crust and urban areas usually have similar spectral signatures and LST, hence clustered in the same group with high LST of the clay class. In addition, there is a clear correlation between the other classes showing the effect of shallow groundwater on barren lands and the rest of the classes with lower LST values. Barren land also exhibited the highest LST value due to the increased accumulation of sandy soil. Wetlands, salinization, and agricultural processes suffered from environmental land degradations resulted from increased water levels associated with decreasing LST values. Therefore, the land conversion from vegetation to urban and saline soils depicts a high LST value and vice versa.

Declarations

Funding

The authors wish to acknowledge the funding support provided by the Science and Technology Development Fund (STDF), Ministry of Higher Education and Scientific Research, Egypt -project number 25757, which has made this research possible.

Competing interests

The authors have no relevant financial or non-financial interests to disclose.

Author Contributions

All authors (Basma M.H. Mansour) & (Mohamed O. Arnous) contributed to the study conception, design, material preparation, data collection, analysis, and interpretation. All authors commented on previous versions of the manuscript. All authors read and approved the final manuscript and approved the version

to be published; and agree to be accountable for all aspects of the work in ensuring that questions related to the accuracy or integrity of any part of the work are appropriately investigated and resolved.

Ethical Approval

Not applicable.

Consent to participate

Not applicable.

Consent to publish

Not applicable.

Availability of data and materials

Not applicable.

References

1. Aboulela H (1994) A study on the tectonic activity and seismicity in the Suez Canal region. M. Sc. Thesis, Fac. Sci., Suez Canal Univ., Ismailia. 133 P
2. Anandababu D, Purushothaman BM, Babu S (2018) Estimation of land surface temperature using LANDSAT 8 data. *International Journal of Advanced Research, Ideas and Innovation in Technology* 4:2. <https://www.ijariit.com>
3. Andersen HS (1996) Estimation of precipitable water vapour from NOAAVHRR during the Hapex Sahel experiment. *Int Remote Sens* 17:2783–2801
4. Arnous MO, Green DR (2015) Monitoring and assessing waterlogged and salt-affected areas in the Eastern Nile Delta region, Egypt, using remotely sensed multi-temporal data and GIS. *J Coast Conserv* 19(3):369–391. DOI 10.1007/s11852-015-0397-5
5. Arnous MO, Hassan MAA (2015) Heavy metals risk assessment in water and bottom sediments of the eastern part of Lake Manzala, Egypt, based on remote sensing and GIS. *Arab J Geosci* 8(10):7899–7918. DOI 10.1007/s12517-014-1763-6
6. Arnous MO, Omar AE (2018) Hydrometeorological hazards assessment of some basin in Southwestern Sinai area, Egypt. *Journal of Coastal Conservation* 22(4):721–743. doi 10.1007/s11852-018-0604-2
7. Arnous MO, Aboulela HA, Green DR (2011) Geo-environmental hazards assessment of the north western Gulf of Suez, Egypt. *J Coast Conserv* 15(1):37–50. DOI 10.1007/s11852-010-0118-z
8. Arnous MO, El-Rayes AE, Green DR (2015) Hydrosalinity and environmental land degradation assessment of the East Nile Delta region, Egypt. *J Coast Conserv* 19(4):491–513. DOI 10.1007/s11852-015-0402-z

9. Arnous M, Geriesh MH, Shendi E, Mansour B (2020) : Appraisal of land degradation and land-use / land-cover change for sustainable development of Suez Canal region, Egypt: Utilizing Remote Sensing and GIS, The 13th International Geological Conference, Jeddah, Saudi Arabia
10. Arnous MO, Thesis PhD (2004) Geology Dept., Fac. of Science, Suez Canal Univ., Ismailia, 283p
11. Arnous MO (2016) Groundwater potentiality mapping of hard-rock terrain in arid regions using geospatial modelling: example from Wadi Feiran basin, South Sinai, Egypt. *Hydrogeol J* 24(6):1375–1392. DOI 10.1007/s10040-016-1417-8
12. Arnous MO, El-Rayes AE, Helmy AM (2017) Land-use / land-cover change: A key to understanding land degradation and relating environmental impacts in Northwestern Sinai. *Egypt Environmental Earth Sciences* 76(7):26. DOI 10.1007/s12665-017-6571-3
13. Badawy A (1996) Seismicity and kinematic evolution of the Sinai plate. PhD thesis, L. Eotvos Univ. Budapest, pp.115
14. Cammalleri C, Vogt J (2015) On the role of Land Surface Temperature as proxy of soil moisture status for drought monitoring in Europe. *Remote Sens* 7:16849–16864
15. Choudhury D, Das K, Das K, A (2019) Assessment of land use land cover changes and its impact on variations of land surface temperature in Asansol-Durgapur Development Region. *Egypt J Remote Sens Sp Sci* 22:203–218
16. Coskun HG, Alganci U, Usta G (2008) Analysis of land use change and urbanization in the Kucukcekmece water basin (Istanbul, Turkey) with temporal satellite data using remote sensing and GIS. *Sensors* 8:7213–7223
17. Czajkowski KP, Goward SN, Mulhern T, Goetz SJ, Waltz A, Shirey D, Stadler S, Prince SD, Dubayah RO (2004) Estimating environmental variables using thermal remote sensing. *thermal remote sensing in Land Surface Processes*. CRC Press, Boca Raton, FL, USA, p 464
18. Dubayah RO, Wood EF, Engman TE, Czajkowski KP, Zion M (2000) A remote sensing approach to macroscale hydrological modelling. In: Schultz G, Engman E (eds) *Remote Sensing in Hydrology and Water mangement*. Springer-Verlag, Berlin, pp 85–102
19. Egyptian Meteorological Authority, Cairo E (2006) *International Journal of Meteorology* 31:308
20. Ehrlich D, Estes JE, Sing A (1994) Applications of NOAA-AVHRR 1km data for environmental monitoring. *Int J Remote Sens* 15:145–161
21. El-Rayes AE, Arnous MO, Aziz AM (2017) Morphotectonic controls of groundwater flow regime and relating environmental impacts in Northwest Sinai, Egypt. *Arab J Geosci* 10:401. DOI 10.1007/s12517-017-3188-5
22. Geriesh MH, Mansour BMH, Farouk H (2019) Assessment of drinking water quality along Port Said Canal treatment plants, Suez Canal corridor, Egypt. *Arab J Geosci* 12:738. <https://doi.org/10.1007/s12517-019-4875-1>
23. Geriesh MH, El-Rayes AE, Gomaah RM, Kaiser MF, Abdelaleem M (2015) : Geoenvironmental Impact Assessment of El-Salam Canal on the Surrounding Soil and Groundwater Resources, North-Western

- Sinai, Egypt. 6 International Conference of Egyptian Society of Environmental Sciences, ESES, Ismailia, 4-6 March 2015
24. Geriesh MH (2004) : Land degradation and soil salinization due to water logging in the newly reclaimed areas, East of Bitter Lakes, Sini Peninsula, Egypt. 7th Conf. Geol. Sinai Develop., Ismailia, Egypt, pp. 23-40
 25. Geriesh MH, Balke KD, El-Rayes AE, Mansour BM (2015) Implications of climate change on the groundwater flow regime and geochemistry of the Nile Delta, Egypt. *J Coast Conserv* 19:589–608. <https://doi.org/10.1007/s11852-015-0409-5>
 26. Ghodeif KO, Arnous MO, Geriesh MH (2013) Define a protected buffer zone for Ismailia Canal, Egypt using Geographic Information Systems. *Arab J Geosci* 6(1):43–53. DOI 10.1007/s12517-011-0326-3
 27. Hagag W (2016) Structural evolution and Cenozoic tectonostratigraphy of the Cairo-Suez district, north Eastern Desert of Egypt: Field-structural data from Gebel Qattamiya-Gebel Um Reheiat area. *J of African Earth Science* 118:174–191
 28. Harbaugh JW, Merriam DF (1968) Computer application in stratigraphic analysis. John Wiley & Sons, New York, p 282
 29. Hashim N, Ahmad A, Abdullah M (2007) Mapping urban heat island phenomenon, remote sensing approach. *Journal-The Institution of Engineers, Malaysia* 68:25–30
 30. Hassan AM, Belal AA, Hassan MA, Farag FM, Mohamed ES (2019) Potential of thermal remote sensing techniques in monitoring waterlogged area based on surface soil moisture retrieval. *J Afr Earth Sc* 155:64–74
 31. Haylemariyam MB (2018) Detection of land surface temperature in Relation to land use land cover change: Dire Dawa City, Ethiopia. *Journal of Remote Sensing & GIS* 7(3):1. DOI: 10.4172/2469-4134.1000245
 32. Heinemann S, Siegmann B, Thonfeld F, Javier Muro J, Jedmowski C, Kemna A, Kraska A, Muller T, Schultz O, Udelhoven J, Wilke T, Rascher N, U (2020) Land Surface Temperature Retrieval for Agricultural Areas Using a Novel UAV Platform Equipped with a Thermal Infrared and Multispectral Sensor. *Remote Sens* 12:1075. doi:10.3390/rs12071075
 33. Holmes A (1965) Principles of physical geology, 2nd edn. Thomas Nelson Ltd, Edinburgh, p 1288
 34. Hua AK, Ping OW (2018) The influence of land-use/land-cover changes on land surface temperature: a case study of Kuala Lumpur metropolitan city. 51:1049–10691
 35. Igun E, Williams M (2018) Impact of urban land cover change on land surface temperature. *Global Journal of Environmental Science and Management* 4:47–58
 36. Jiang J, Tian G (2010) Analysis of the impact of land use/land cover change on land surface temperature with remote sensing. *Procedia Environ Sci* 2:571–575
 37. Kalma JD, McVicar TR, McCabe MF (2008) Estimating land surface evaporation: A review of methods using remotely sensed surface temperature data. *Surv Geophys* 29:421–469

38. Kuenzer C, Guo H, Ottinger M, Zhang J, Dech S (2013) Space borne Thermal Infrared Observations - An overview of most frequently used sensors for applied research. In Thermal Infrared Remote Sensing: Sensors, Methods, Applications; Springer: Berlin, Germany, 2013; pp. 131-148
39. Li ZL, Tang BH, Wu H, Ren H, Yan G, Wan Z, Trigo IF, Sobrino JA (2013) Satellite-derived land surface temperature: Current status and perspectives. *Remote Sens Environ* 131:14–37
40. Lilly Rose A, Devadas MD (2009) : Analysis of land surface temperature and land use/land cover types using remote sensing imagery-a case in Chennai city, India. In The seventh International Conference on Urban Clim
41. Mahmood R, Pielke Sr RA, Hubbard KG, Niyogi D, Bonan G et al (2010) Impacts of land use/land cover change on climate and future research priorities. *Bull Am Meteorol Soc* 91:37–46
42. Mallick J, Kant Y, Bharath BD (2008) Estimation of land surface temperature over Delhi using Landsat-7 ETM+J. *Ind Geophys Union* 12(3):131–140
43. Mansour BMH (2015) : Climatic and human impacts on the hydrogeological regime of East Nile Delta, Egypt. Ph. D. Thesis, Faculty of Science, Suez Canal University, Ismailia, Egypt
44. Moubarak AH, Arnous MO, El-Rayes (2020) : Integrated Geoenvironmental and Geotechnical Risk Assessment of East Port Said Region, Egypt for Regional Development. *Geotechnical and Geological Engineering*, DOI: 10.1007/s10706-020-01571-4
45. Pal S, Ziaul S (2017) Detection of land use and land cover change and land surface temperature in English Bazar urban centre. *The Egypt J Remote Sens Space Sci* 20(1):125–145
46. Prince SD, Goward SN (1995) Global primary production: A remote sensing approach. *J Biogeogr* 22:815–835
47. Sahana M, Ahmed R, Sajjad H (2016) Analyzing land surface temperature distribution in response to land use/land cover change using split window algorithm and spectral radiance model in Sundarban Biosphere Reserve, India. *Modeling Earth Systems and Environment* 2:81
48. Said R (1962) *The geology of Egypt*. Elsevier Publishing Co., Amsterdam, New York
49. Smith C (1984) Well evaluation conference in Schlumberger, Egypt
50. Sun H, Zhou B, Liu H (2019) Spatial evaluation of soil moisture (SM), land surface temperature (LST), and LST-derived sm indexes dynamics during SMAPVEX12. *Sensors*,19,1247
51. Sun Q, Wu Z, Tan Z, J (2012) The relationship between land surface temperature and land use/land cover in Guangzhou, China. *Environ Earth Sci* 65:1687–1694
52. Susskind J, Piraino P, Rokke L, Mehta IL, A (1997) Characteristics of the TOVS Pathfinder path A data set. *Bull Am Meteorol Soc* 78:1449–1472
53. Tali JA, Divya S, Murthy K (2013) Influence of urbanisation on the land use change: A case study of Srinagar City. *Am J Res Commun* 1(7):271–283
54. United Nations (2010) *World Urbanization Prospects: The 2009 Revision*; Population Division. Department of Economic and Social Affairs UN, New York, NY, USA

55. Weng Q, Lu D, Liang B (2006) Urban surface biophysical descriptors and land surface temperature variations. *Photogramm Eng Remote Sens* 72:1275–1286
56. Weng Q, Lu D, Schubring J (2004) Estimation of land surface temperature–vegetation abundance relationship for urban heat island studies. *Remote Sens Environ* 89(4):467–483
57. Xiao RB, Ouyang ZY, Zheng H, Li WF, Schienke EW, Wang XK (2007) Spatial patterns of impervious surfaces and their impact on land surface temperature in Beijing. *China J Environ Sci* 19:250–256
58. Xiaolu Zhou and Yi-Chen Wang (2010) Dynamics of land surface temperature in response to land-use/cover change. *Geographic research journal* DOI. /10.1111/j.1745-5871.201000686.x
59. Zhang F, Tiyp T, Kung H, Johnson VC, Maimaitiyiming M, Zhou M, Wang J (2016) Dynamics of land surface temperature (LST) in response to land use and land cover (LULC) changes in the Weigan and Kuqa river oasis, Xinjiang, China. *Arab J Geosci* 9(7):1–14
60. Zhang HK, Huang B, Zhang M, Cao K, Yu L (2015) A generalization of spatial and temporal fusion methods for remotely sensed surface parameters. *Int J Remote Sens* 36(17):4411–4445
61. Zhang Y, Odeh IO, Ramadan E (2013) Assessment of land surface temperature in relation to landscape metrics and fractional vegetation cover in an urban/peri-urban region using Landsat data. *Int J Remote Sens* 34(1):168–189
62. Zhang X, Estoque RC, Murayama Y (2017) An urban heat island study in Nanchang City, China based on land surface temperature and social-ecological variables. *Sustainable Cities and Society* 32:557–568

Figures

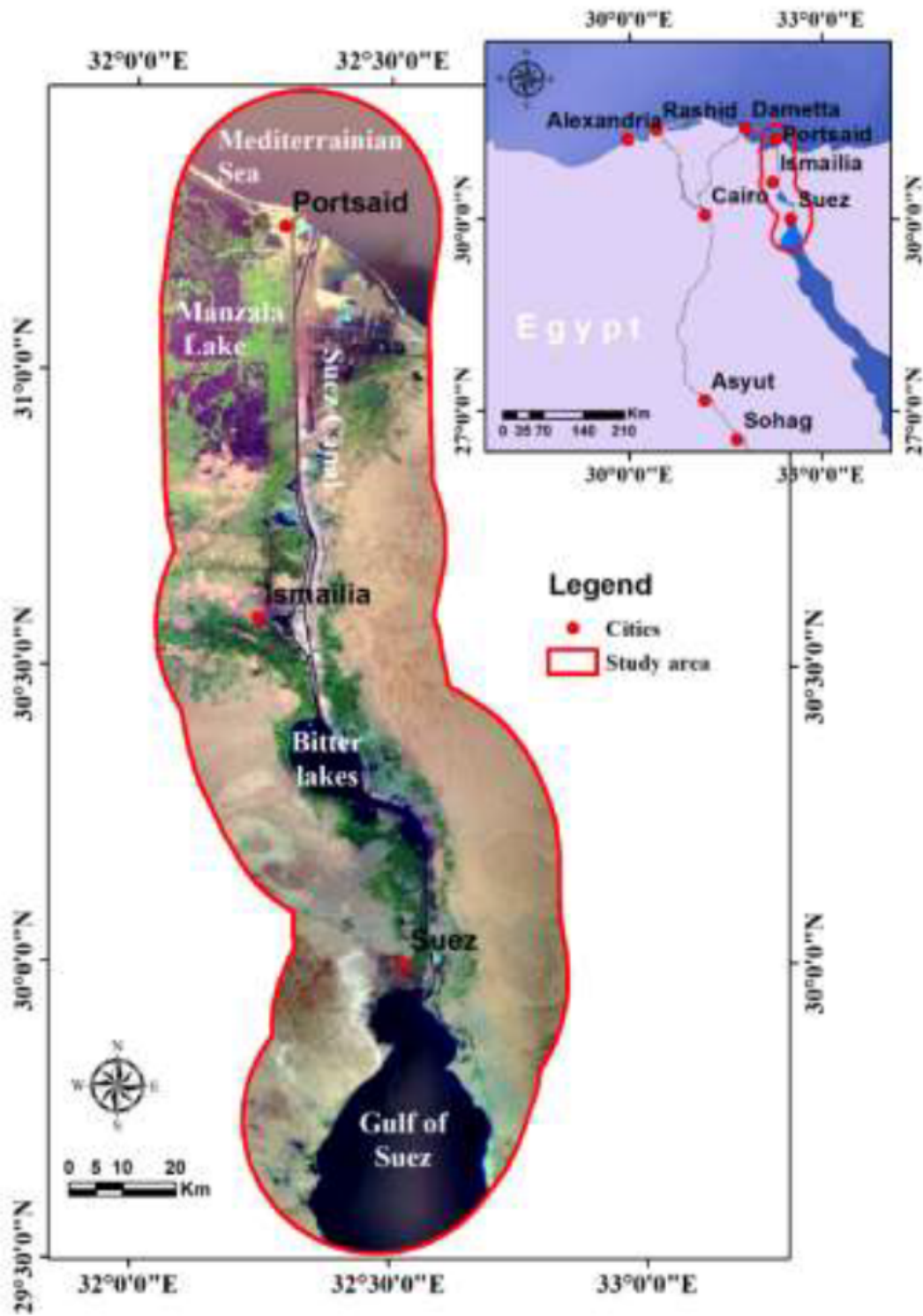


Figure 1

The location map of the Suez Canal region (SCR).

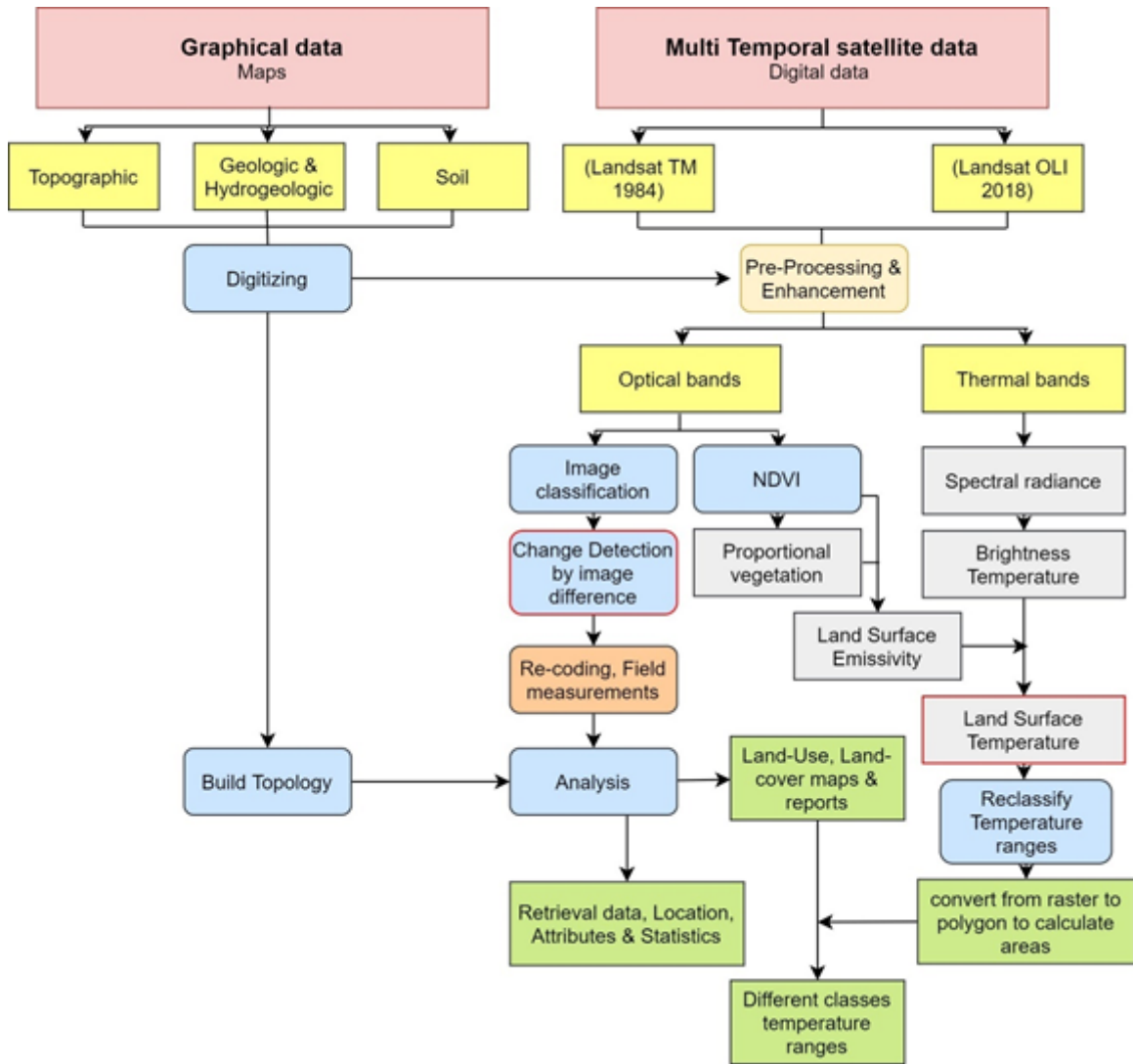


Figure 2

Methods used to reach the study aim.

Figure 3

Multi-temporal data is represented by three full scenes of each a) TM+4 and b) OLI+8.

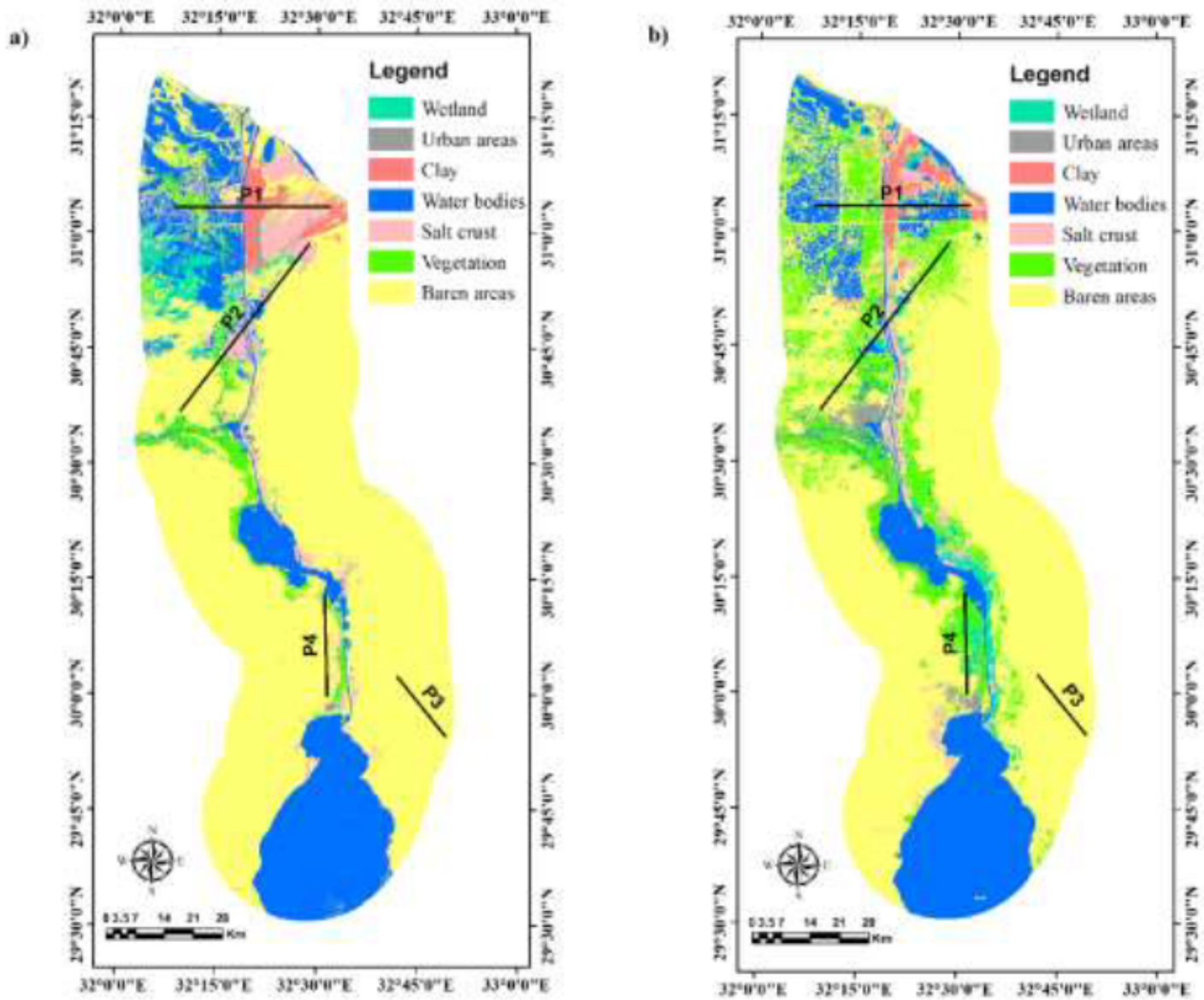


Figure 4

LULC classification of the study area for the years a) 1984 and b) 2018.

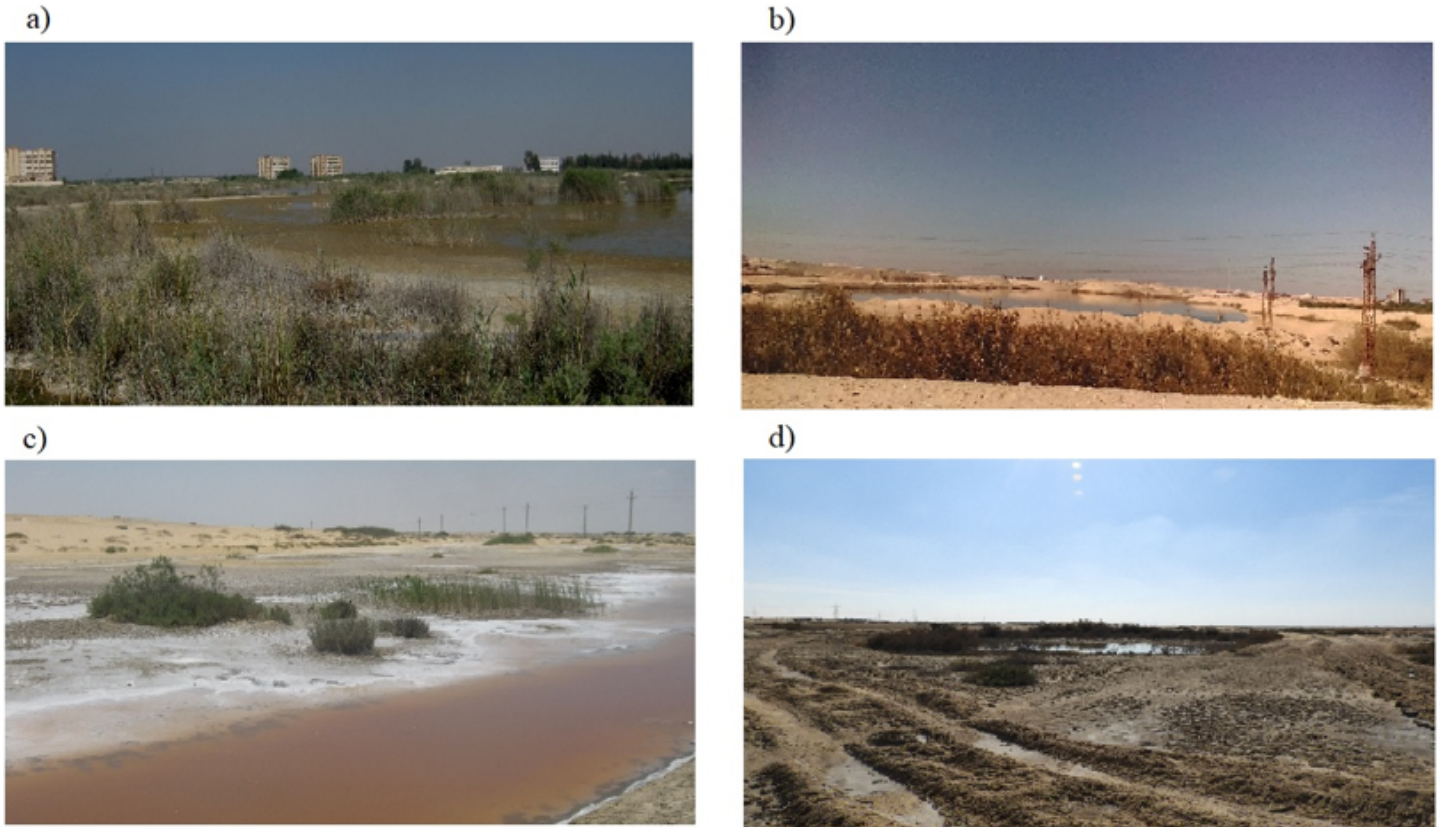


Figure 5

Some environmental and land degradation hazards found in SCR such as waterlogging and salinization at a) El-Ballah area, b) eastern bitter lake between sand dunes, c) northern lowlands, and d) along the Suez Canal.

Figure 6

Calculated LST in degree centigrade of the study area for the years a) 1984 and b) 2018 and the results of change detection c).

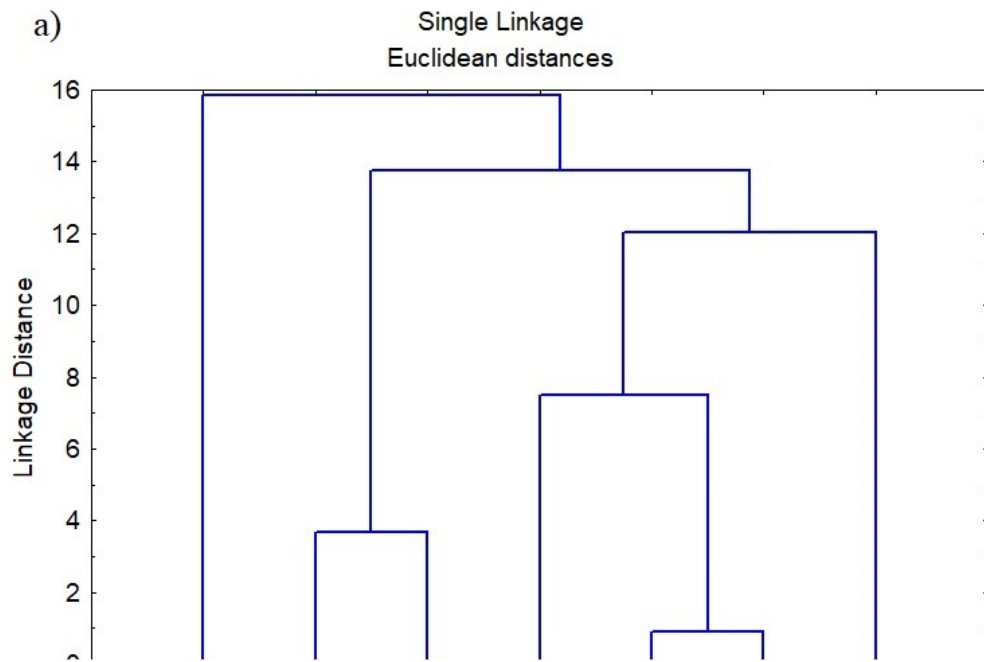


Figure 7

Cluster analysis of LULC classes in the study area for the years a) 1984 and b) 2018.

Figure 8

Cross-sections produced across the SCR area to represent LST variations between all major classes with the LULC transformation as a land surface reflection for 1984 and 2018.

Figure 9

Hot spots taken across the SCR area.

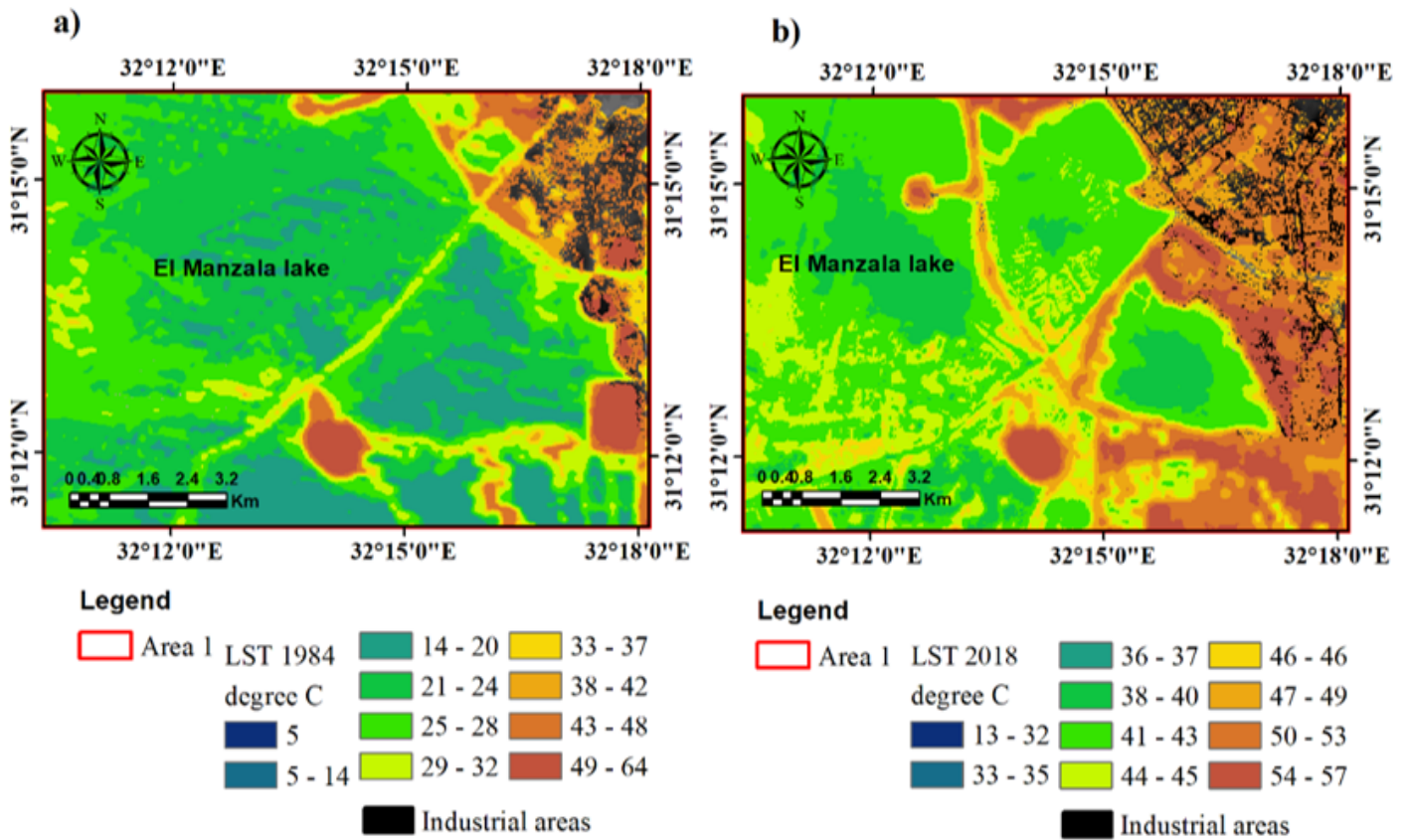


Figure 10

Hot spot 1 taken across the SCR area for a) 1984 and b) 2018.

Figure 11

Hot spot 2 taken across the SCR area for a) 1984 and b) 2018.

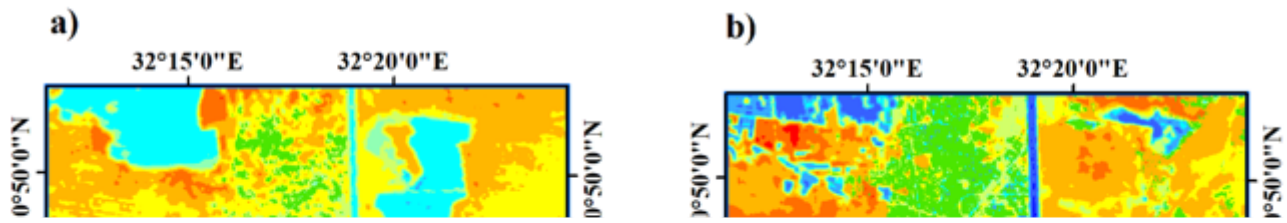


Figure 12

Hot spot 3 taken across the SCR area for a) 1984 and b) 2018.

Figure 13

Hot spot 4 taken across the SCR area for a) 1984 and b) 2018.

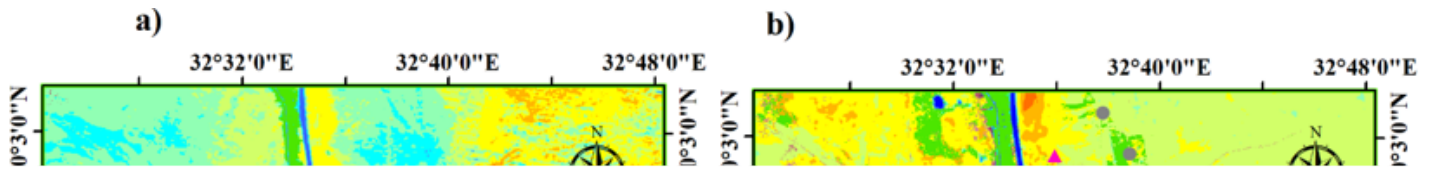


Figure 14

Hot spot 5 taken across the SCR area for a) 1984 and b) 2018.

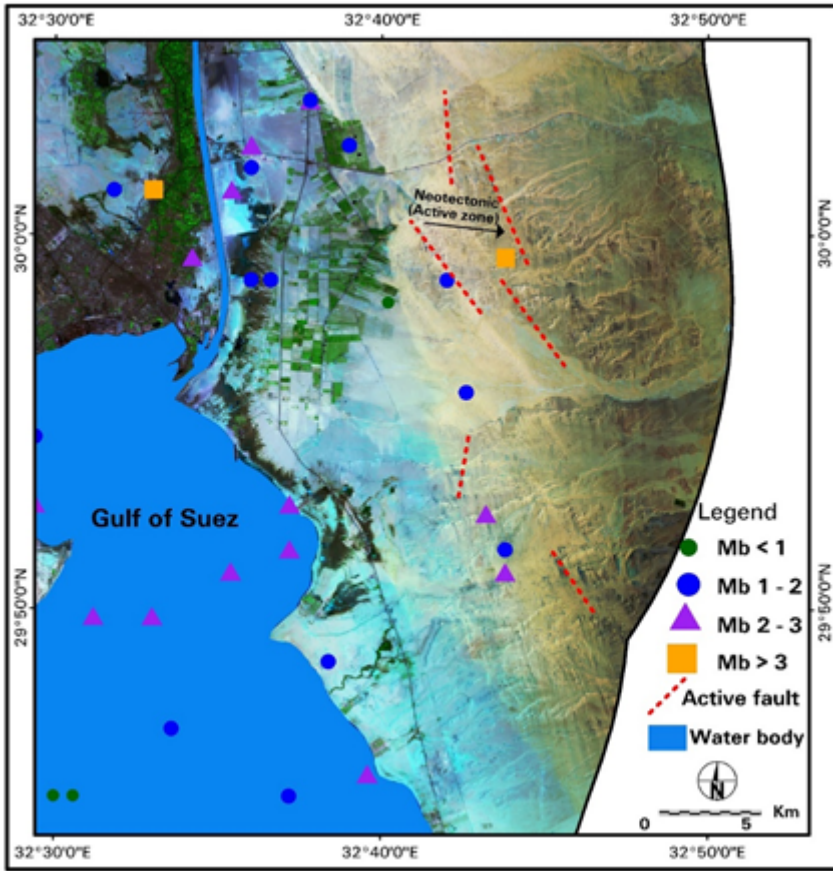


Figure 15

Integrated remote sensing data and seismic data to show some prints related to the seismic activity and neo-tectonic

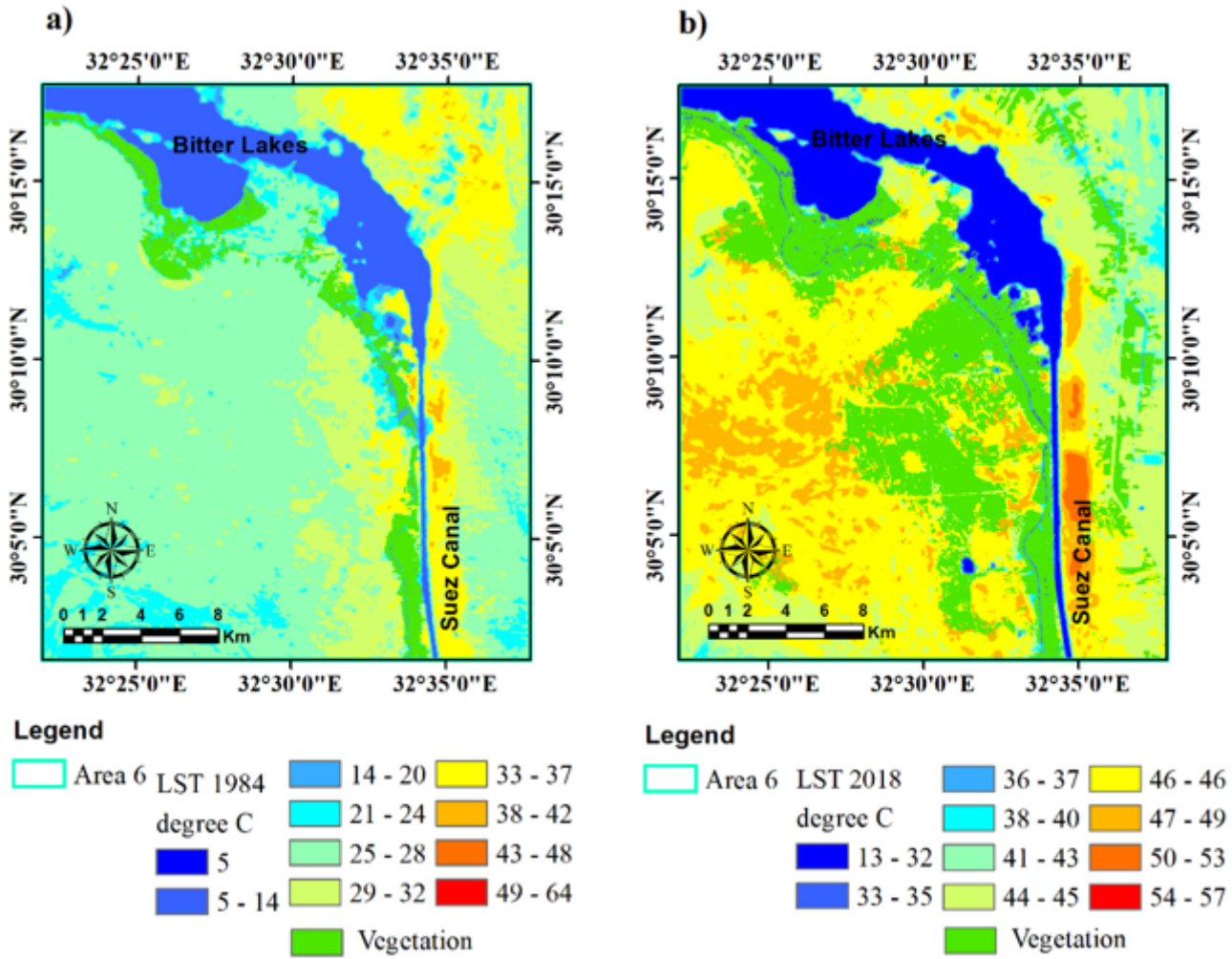


Figure 16

Hot spot 6 taken across the SCR area for a) 1984 and b) 2018.

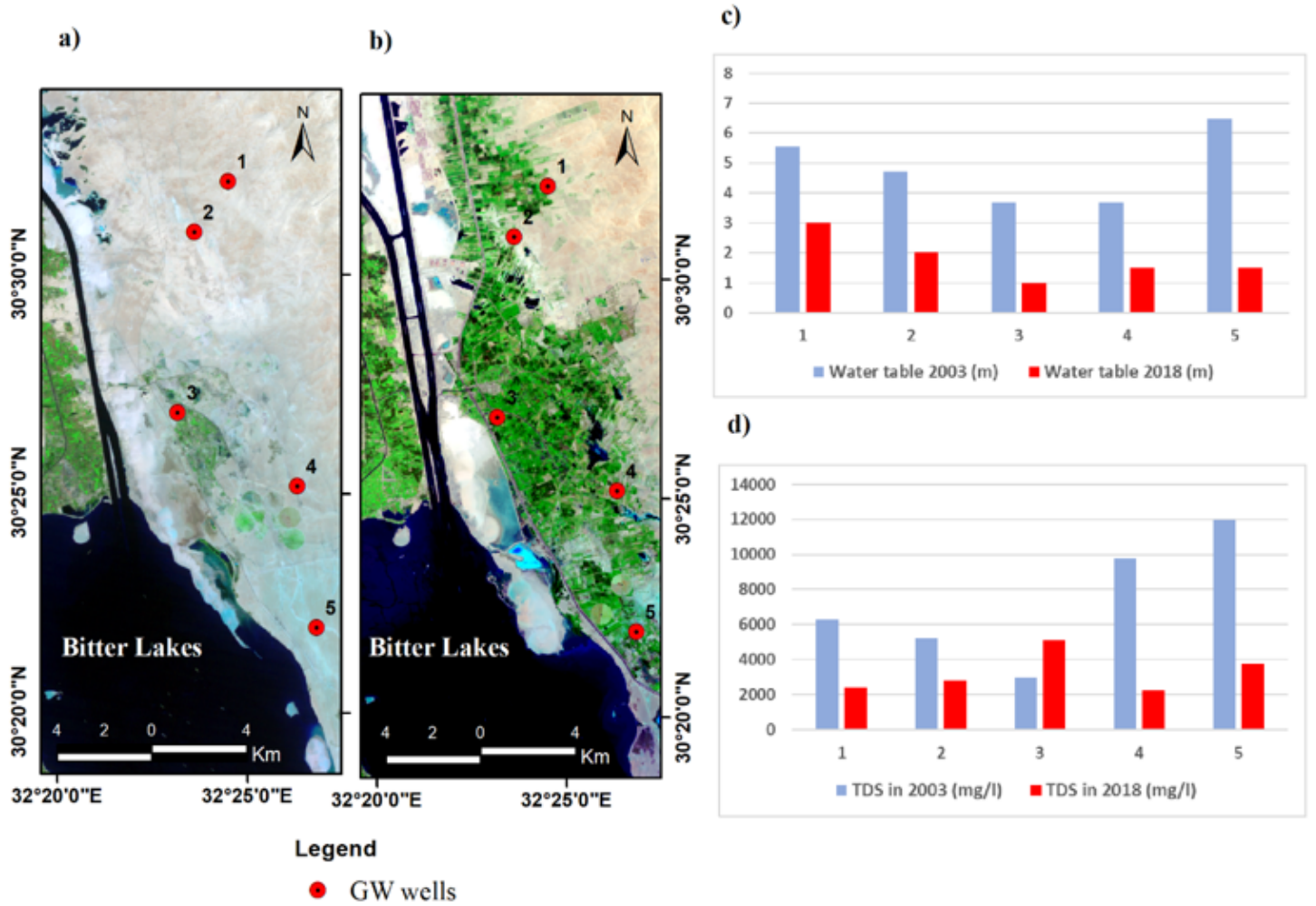


Figure 17

The change in groundwater levels (c) and salinity (d) across the SCR area from a) 2003 to b) 2018.